Effects of ambient air on the characteristics of an atmospheric-pressure plasma jet of a gas mixture of highly N_2-diluted O_2 on a sliding substrate

Tatsuru Shirafuji, Yasushi Sawada

Effects of ambient air on the characteristics of an atmospheric-pressure plasma jet of a gas mixture of highly N_2-diluted O_2 on a sliding substrate

Tatsuru Shirafuji*[1,2] and Yasushi Sawada[3]

[1] *Department of Physical Electronics and Informatics, Osaka City University, Osaka 558-8585, Japan*
[2] *Water Frontier Science and Technology Research Center (W-FST), Research Institute for Science and Technology, Tokyo University of Science, Shinjuku, Tokyo 162-8601, Japan*
[3] *Air Water R&D Co., Ltd., Sakai 592-8331, Japan*

We have performed numerical simulations of reaction kinetics and flow dynamics of an atmospheric-pressure plasma jet (APPJ) of a gas mixture of 99.9% N_2 and 0.1% O_2 in a two-dimensional flow channel with a height of 5 mm and investigated the effects of a sliding substrate and the substitution of the ambient gas. The sliding substrate in the flow channel produces the gas-drag effect, which results in not only the bending of the APPJ trajectory but also significant loss of atomic oxygen when the ambient gas is air. The flux of atomic oxygen integrated on the substrate is reduced to 19% of that integrated on the fixed substrate. We discuss the mechanisms of the reduction in the atomic oxygen flux through the analysis of spatial distributions of atomic oxygen loss reactions and show that the reduction in the atomic oxygen flux can be suppressed by substituting the ambient gas (air) with N_2.

1. Introduction

Atmospheric-pressure plasma jets (APPJs) have been widely used in various surface treatment processes such as for wettability improvement,[1)] adhesion improvement,[2)] cleaning,[3)] and photoresist ashing.[4,5)] Numerical simulations of APPJ processes have been extensively performed and have revealed the discharge physics, chemical reactions, and gas-flow dynamics involved in the APPJ processes.[6–9)] Most of the simulation models, however, are based on a laboratory-scale APPJ process, in which an APPJ is effused from a cylindrical discharge tube with a diameter of approximately 5 mm, and the substrate being subjected to the APPJ does not move.

On the other hand, an industrial-scale surface treatment is often performed in a roll-to-roll process,[10)] in which a sheet-type APPJ is irradiated on a sliding substrate. In such a process, we must pay attention to the fact that a sliding substrate drags gaseous species in contact with

*E-mail: sirafuji@elec.eng.osaka-cu.ac.jp

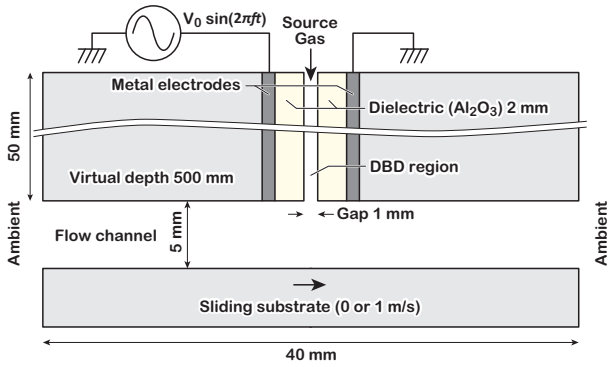

Fig. 1. (Color online) Schematic illustration of the geometrical model used for the numerical simulation in this work.

its surface. The gas-drag effect carries gaseous species away from the APPJ-irradiated area and replaces them with ambient gases, which may alter the gas-phase or surface chemistry from those of a fixed substrate. The gas-drag effect, however, has never been taken into account in numerical simulations of APPJs, to the best of our knowledge. Thus, we performed numerical simulations of an APPJ in contact with a sliding substrate. Since APPJs can be applied to the treatments of liquids,[11,12] the model proposed in this work may also be used for understanding the APPJ treatment of a flowing liquid medium.

2. Model description

2.1 Geometrical model and condition

The geometrical model used in our simulation consists of a two-dimensional (2D) flow channel equipped with a dielectric barrier discharge (DBD) system, as shown in Fig. 1. The gap of the flow channel is 5 mm. The bottom boundary of the flow channel is treated as a substrate sliding toward the right-hand side at a velocity of 1 or 0 m/s, and is used for comparison. The sliding velocity of 1 m/s was chosen on the basis of practical surface treatments using an atmospheric-pressure plasma.[10] An APPJ is injected from the DBD region located at the center of the top boundary of the flow channel. The DBD region consists of a gas gap with a width of 1 mm, sandwiched by two dielectrics made of Al_2O_3 with a thickness of 2 mm and a relative permittivity of 9.5. The two metal electrodes in the DBD region are assumed to be perfect conductors with a thickness of 1 mm. The height of the DBD region is 50 mm. Although the DBD region in our simulation is treated as a 2D geometry, we have assumed a virtual depth of 500 mm in the DBD region, because some volume of the DBD region is necessary for calculating the mean residence time of gaseous species passing through the DBD region.

The discharge gas is a mixture of 0.1% O_2 and 99.9% N_2, and is fed into the top gas gap of the DBD system. This relatively high dilution of the source gas with N_2 is used to obtain a higher number density of atomic oxygen.[4] The gas temperature in the whole geometry is assumed to be 400 K because the temperature of the gas that effused from the nozzle was approximately 400 K in the actual system corresponding to Fig. 1. The flow rate of the gas mixture is 300 L/min at this temperature, and results in a flow velocity of 10 m/s. The mean residence time of the gaseous species in the DBD region is 5 ms. The ambient gas in this work is air (80% N_2 and 20% O_2) or 100% N_2, which is used for comparison. The voltage applied to the metal electrode on the left-hand side is given by $V_0 \sin(2\pi f t)$, where t is time, the amplitude V_0 is 3 kV, and the frequency f is 50 kHz. The period of one cycle is 20 μs. The metal electrode on the right-hand side is grounded.

2.2 Simulation modules

We employed three modules for simulation in this work. The first module is for one-dimensional (1D) simulation in the DBD region. This module deals with 1D horizontal phenomena between two dielectric electrodes, which involve the electron impact reactions listed in Table I. This module is referred to as module 1 hereafter. Under the initial condition of module 1, the space charge density and the potential are assumed to be zero. This causes transient and asymmetric spatial profiles in the phenomena to occur in the first few cycles until the calculated results reach their periodic steady states.

Output data from module 1 are spatial profiles of electron-collision reaction frequencies in the DBD region, which are used in module 2 described below. Reaction frequency is defined by the reaction rate divided by the number density of a parent molecule. For example, the reaction frequency for E8 is given by

$$\frac{1}{2}\,\frac{d[\mathrm{O}]}{dt}\,\frac{1}{[\mathrm{O}_2]}, \tag{1}$$

where [O] and [O_2] are the number densities of atomic and molecular oxygen. The factor $1/2$ is multiplied because reaction E8 produces two oxygen atoms at the same time. The frequencies of all the electron-collision reactions are obtained by solving rate equations for the reactions listed in Table I together with Poisson's equation and drift-diffusion equations. Electron impact reaction rates are calculated by Boltzmann analysis[18] using electron-collision cross-sectional data for N_2 and O_2 together with the electric field obtained by solving Poisson's equation. Since the time scale of 20 μs for the DBD is $1/250$ of the mean residence time of 5 ms, we have neglected the gas-flow dynamics and secondary reactions of neutral species

Table I. Electron impact reactions considered for the DBD region. The species in their specific energy states are abbreviated as O = O(^{3}P), N = N(^{4}S), $N_2(A) = N_2(A^3\Sigma)$, $O_2(a) = O_2(a^1\Delta)$, and $O_2(b) = O_2(b^1\Sigma)$.

No.	Reactants		Products	Process	Refs.
E1	$e + N_2$	$\rightarrow$	$e + N_2$	Momentum transfer	13, 14
E2	$e + N_2$	$\rightarrow$	$e + e + N_2^+$	Ionization	13, 14
E3	$e + N_2$	$\rightarrow$	e + N + N	Dissociation	14, 15
E4	$e + N_2$	$\rightarrow$	$e + N_2$	Vibrational excitation ($\Delta\varepsilon$ = 0.291 eV)	13, 14
E5	$e + N_2$	$\rightarrow$	$e + N_2(A)$	Electronic excitation ($\Delta\varepsilon$ = 6.17 eV)	13, 14
E6	$e + O_2$	$\rightarrow$	$e + O_2$	Momentum transfer	16, 17
E7	$e + O_2$	$\rightarrow$	$e + e + O_2^+$	Ionization	16, 17
E8	$e + O_2$	$\rightarrow$	e + O + O	Dissociation through excitation to $A^3\Sigma_u^+$	16, 17
E9	$e + O_2$	$\rightarrow$	e + O(^{1}D) + O	Dissociation through excitation to $B^3\Sigma_u^-$	16, 17
E10	$e + O_2$	$\rightarrow$	$e + O_2(a)$	Electronic excitation	16, 17
E11	$e + O_2$	$\rightarrow$	$e + O_2(b)$	Electronic excitation	16, 17
E12	$e + O_2$	$\rightarrow$	O_2^-	Attachment	17
E13	$e + O_2$	$\rightarrow$	O + O−	Dissociative attachment	17

in module 1. The time division Δt for module 1 is 5 ns. The number of spatial divisions is 201, where the width of a division near the surface is much smaller than that at the center. The minimum width of the spatial division on the surface is 2 μm and the maximum width of the spatial division at the center is 10 μm. Spatial profiles of electron-collision reaction rates reach their periodic steady states after calculating for 3 or 4 cycles of the DBD, as described below, the actual time for which is 60 or 80 μs.

Note that module 1 is constructed under several assumptions. Regarding O(^{1}D), we have assumed that it is immediately converted to ground-state atomic oxygen through the following reactions:[19)]

$$O(^1D) + O_2 \rightarrow O + O_2, \qquad (4 \times 10^{-11}\ \mathrm{cm}^3/\mathrm{s}), \tag{2}$$

$$O(^1D) + N_2 \rightarrow O + N_2, \qquad (3 \times 10^{-11}\ \mathrm{cm}^3/\mathrm{s}), \tag{3}$$

because of high collision frequency at atmospheric pressure.

Regarding the spatial profile of the discharge between the electrodes, the actual DBD includes spatially inhomogeneous filamentary discharge. Our present model, however, assumes spatially uniform discharge between the electrodes because the simulation of 2D or 3D filamentary discharges requires a very long computation time.[20–22)] In the case of filamentary discharges, electron collision dissociation of molecules occurs only at the positions where filamentary discharge occurs. In other positions, the source gas passes through without being

affected by electron collisions. Because of this assumption, our model may overestimate the number density of radicals generated in the DBD region. However, since the purpose of this study is not the exact prediction of radical density, we have assumed a uniform discharge between the electrodes.

The number densities of the parent molecules N_2 and O_2 are assumed to be independent of the vertical position in the DBD region. Since the parent molecules dissociate as they pass between the electrodes, one might have concerns about the reduction in the number densities of the parent molecules. However, under the present discharge condition, the degree of dissociation of the parent molecules is very small, as shown by the results for module 2 described below. This means that we can assume that the number densities of the parent molecules are constant in the entire DBD region.

Although the number densities of the parent molecules are almost constant, additional neutral species such as O_3, NO, NO_2, and N_2O will be generated by secondary reactions as the parent molecules pass through the DBD region. Since the initial electron energy distribution function (EEDF) in the DBD region is governed by the 99.9% N_2 and 0.1% O_2, these additional species may modify the EEDF from that under the initial condition, and consequently alter the chemistry downstream of the DBD region.[23–25] However, as described below, the number densities of the additional neutral species are much lower than those of the parent molecules N_2 and O_2. Under such a condition, we can neglect the effect of additional species on the EEDF.[21] Thus, we have assumed that EEDF in the DBD region is governed only by the parent molecules N_2 and O_2.

Regarding the spatial velocity profile in the DBD region, it is assumed to be laminar. The Reynolds number (*Re*) under the present condition is 383, which is calculated using the following equation:[26]

$$Re = \frac{\rho\, Q}{(w_0 + h_0)\, \eta}, \tag{4}$$

where ρ is the fluid density, Q (= 300 L/min = 0.005 m^3/s) is the volumetric flow rate, w_0 (= 500 mm) is the width of the DBD region, h_0 (= 1 mm) is the gap of the DBD region, and η is the absolute viscosity of the fluid. Since 99% of the fluid in the DBD region is N_2, we can use ρ = 0.853 kg/m^3 and η = 22.25 μPa·s for N_2 at the operation temperature of 400 K.[27] The resulting *Re* of 383 is below the critical value of 1,400 to maintain laminar flow in a flow system, which allows us to treat the flow in the DBD region as laminar.

The second module, which is hereafter referred to as module 2, is also for 1D simulation in the DBD region. However, it solves only rate equations for neutral species to deal with

phenomena on longer time scales than that of module 1. Ten seconds has been chosen as the maximum time for module 2 to reach the steady-state concentration of gas-phase species. Since 10 s corresponds to 50,000 cycles in module 1, the calculation will not finish within a reasonable time if we apply module 1 for this time scale. Thus, we have employed the simplified module 2. The time division Δt in module 2 is variable and is given by $\Delta t = 10^k$ s, where k is increased from -9 to 1 in steps of 0.01. The number of spatial divisions is 101, where the width of a division near the surface is much smaller than that at the center. The minimum width of the spatial division on the surface is 4 μm and the maximum width of the spatial division at the center is 20 μm.

The reactions involved in module 2 are those listed in Table II and the electron-collision reactions involving the production of neutral species, which are E3, E5, E8, E9, E10, E11, and E13 in Table I. Although the plasma chemistry in the gas mixture of N_2 and O_2 is constructed of hundreds of reactions involving neutral species,[19] we have considered the reactions up to the formation of N_2O_5 in accordance with the compilation by Becker et al.[48] The rates of the latter electron-collision reactions are given as averages of their reaction rates over one cycle in the periodic steady-state results of module 1, because the slow phenomena solved with module 2 are affected by only the time-averaged results of the fast phenomena dealt with using module 1.

As described below, the number densities of charged species reach their periodic steady states after the calculation of 4 cycles, namely, after 80 μs, in module 1. Thus, we have assumed that the number densities of charged species do not change over the longer period, namely, on the time scale of module 2. However, there must be charge exchange and neutralization reactions between charged species, which may alter the chemistry of neutral species.[21,24,43] This effect is not considered in the present model because we have focused on the kinetics of the species after effusion from the jet nozzle. We will prepare a model involving the charge exchange and neutralization reactions in the future, the results of which will be compared with those obtained in this work.

Gas-flow dynamics are no longer neglected because of the longer time scale in module 2. However, horizontal 1D simulation cannot deal with vertical gas-flow dynamics of inflow and outflow. In module 2, the inflow and outflow are virtually included as the generation and loss terms, respectively, in the rate equation for each species. The generation term is calculated with

$$\left.\frac{dN_i}{dt}\right|_{\text{gen}} = \left(\frac{P_{\text{Gas}} f_i Q_{\text{in}}}{R_{\text{Gas}} T_{\text{Gas}}}\right)\left(\frac{1}{V_{\text{DBD}}}\right), \tag{5}$$

Table II. Secondary reactions considered for the DBD region. Rate coefficients are calculated by $A(T_{Gas}/300)^n \exp(-E_a/(R_{Gas}T_{Gas}))$ unless otherwise noted. The unit for spontaneous deexcitation reactions is 1/s. The species in their specific energy states are abbreviated as O = O(^{3}P), N = N(^{4}S), $N_2(A) = N_2(A^3\Sigma)$, $O_2(a) = O_2(a^1\Delta)$, and $O_2(b) = O_2(b^1\Sigma)$.

No.	Reactants		Products	A (cm^3/s)	n	E_a (kJ/mol)	Refs.
R1	$N_2(A) + O_2$	$\rightarrow$	$N_2 + O + O$	1.50×10^{-12}	0	0	28, 29
R2	$N_2(A) + O_2$	$\rightarrow$	$N_2 + O_2$	8.10×10^{-13}	0	0	28, 30
R3	$O + O_2 + M$	$\rightarrow$	$O_3 + M$	6.01×10^{-34}	-2.8	0	31
R4	$N + O_2$	$\rightarrow$	$NO + O$	1.50×10^{-11}	0	29.93	32
R5	$O + O + M$	$\rightarrow$	$O_2 + M$	5.21×10^{-35}	0	-7.48	33
R6	$N + N + M$	$\rightarrow$	$N_2 + M$	1.38×10^{-33}	0	-4.18	34
R7	$N + O + M$	$\rightarrow$	$NO + M$	5.46×10^{-33}	0	-1.29	35
R8	$N + NO$	$\rightarrow$	$N_2 + O$	2.90×10^{-11}	0	0	36, 37
R9	$N + O_3$	$\rightarrow$	$NO + O_2$	2.01×10^{-16}	0	0	36, 37
R10	$O + NO + M$	$\rightarrow$	$NO_2 + M$	1.00×10^{-31}	-1.6	0	31
R11	$O + O_3$	$\rightarrow$	$O_2 + O_2$	8.00×10^{-12}	0	0	38
R12	$O_3 + NO$	$\rightarrow$	$NO_2 + O_2$	1.40×10^{-12}	0	10.89	38
R13	$O_3 + NO_2$	$\rightarrow$	$NO + O_2 + O_2$	1.00×10^{-18}	0	0	39
R14	$O_3 + NO_2$	$\rightarrow$	$NO_3 + O_2$	1.40×10^{-13}	0	20.54	38
R15	$NO + NO_3$	$\rightarrow$	$NO_2 + NO_2$	1.80×10^{-11}	0	-0.91	38
R16	$NO_2 + N$	$\rightarrow$	$N_2 + O_2$	7.00×10^{-13}	0	0	40
R17	$NO_2 + N$	$\rightarrow$	$N_2 + O + O$	9.10×10^{-13}	0	0	40
R18	$NO_2 + N$	$\rightarrow$	$N_2O + O$	5.80×10^{-12}	0	-1.83	36, 37
R19	$NO_2 + N$	$\rightarrow$	$NO + NO$	6.00×10^{-13}	0	0	40, 41
R20	$NO_2 + NO_2 + M$	$\rightarrow$	$N_2O_4 + M$	1.40×10^{-33}	-3.8	0	38
R21	$NO_2 + NO_3 + M$	$\rightarrow$	$N_2O_5 + M$	2.81×10^{-30}	-3.5	0	31
R22	$NO_2 + O$	$\rightarrow$	$NO + O_2$	5.50×10^{-12}	0	-1.560	38
R23	$NO_2 + O + M$	$\rightarrow$	$NO_3 + M$	9.02×10^{-32}	-2	0	31
R24	$NO_3 + O$	$\rightarrow$	$NO_2 + O_2$	1.70×10^{-11}	0	0	38
R25	$NO_3 + NO_3$	$\rightarrow$	$NO_2 + NO_2 + O_2$	8.50×10^{-13}	0	20.37	36
R26	$NO_3 + NO$	$\rightarrow$	$NO_2 + NO_2$	1.80×10^{-11}	0	-0.91	38
R27	$N_2O_5 + M$	$\rightarrow$	$NO_3 + NO_2 + M$	1.00×10^{-3}	-3.5	91.46	31
R28	$O_3 + O_2(a)$	$\rightarrow$	$O_2 + O_2 + O$	5.20×10^{-11}	0	23.621	19, 42
R29	$O_3 + O_2(b)$	$\rightarrow$	$O_2(a) + O_2(a) + O$	1.80×10^{-11}	0	0	19, 43
R30	$O_3 + O_2(b)$	$\rightarrow$	$O_2 + O_2 + O$	7.33×10^{-12}	0.5	0	44, 45
R31	$O_3 + O_2(b)$	$\rightarrow$	$O_3 + O_2(a)$	7.33×10^{-12}	0.5	0	44, 45
R32	$O_3 + O_2(b)$	$\rightarrow$	$O_3 + O_2$	7.33×10^{-12}	0.5	0	44, 45
R33	$O_2(a) + O_2$	$\rightarrow$	$O_2 + O_2$	2.20×10^{-18}	0.8	0	19, 43
R34	$O_2(a) + N_2$	$\rightarrow$	$O_2 + N_2$	1.40×10^{-19}	0	0	19, 37
R35	$O_2(a) + O_2$	$\rightarrow$	$O_3 + O$	2.96×10^{-21}	0	0	44
R36	$O_2(a) + N$	$\rightarrow$	$O + NO$	2.00×10^{-14}	0	4.989	19, 43

No.	Reactants		Products	A (cm^3/s)	n	E_a (kJ/mol)	Refs.
R37	O_2(a) + O	→	O_2 + O	7.00×10^{-16}	0	0	19, 43
R38	O_2(a) + NO	→	O + NO_2	4.88×10^{-18}	0	0	19, 42
R39	O_2(a) + NO	→	O_2 + NO	2.50×10^{-11}	0	0	19, 43
R40	O_2(a)	→	O_2	2.70×10^{-4} (1/s)	0	0	44, 46
R41	O_2(b) + O_2	→	O_2 + O_2	4.00×10^{-18}	0.5	0	44, 45
R42	O_2(b) + N_2	→	O_2(a) + N_2	4.90×10^{-15}	0	2.104	19, 43
R43	O_2(b) + O_2	→	O_2(a) + O_2	3.60×10^{-17}	0.5	0	44, 45
R44	O_2(b) + O	→	O_2 + O	8.00×10^{-14}	0	0	19, 43
R45	O_2(b) + NO	→	O_2(a) + NO	4.00×10^{-14}	0	0	19, 43
R46	O_2(b)	→	O_2	8.30×10^{-2} (1/s)	0	0	44, 47

where N_i is the number density of the i-th species, P_{Gas} is the gas pressure, Q_{in} is the total flow rate of a source gas, R_{Gas} is the gas constant, T_{Gas} is the gas temperature, and V_{DBD} is the volume of the DBD region. f_i is the molar fraction of the i-th species in the source gas. The loss term is calculated with

$$\left.\frac{dN_i}{dt}\right|_{\mathrm{loss}} = -\frac{N_i}{\tau}, \tag{6}$$

where τ is the mean residence time of 5 ms in the DBD region.

The third module, which is hereafter referred to as module 3, is for 2D simulation in the flow channel. Module 3 solves 2D rate equations together with Navier-Stokes equations, including that of the gas-drag effect caused by the sliding substrate on the bottom of the flow channel. The time division Δt in module 3 is variable and given by $\Delta t = 10^k$ s, where k is varied from -10 to 2 in steps of 0.006. Since we have employed a finite element method, the 2D space is divided by triangular meshes with 20,543 elements. The size of the meshes has been chosen to be much smaller near the nozzle and surface. The minimum length of the side of a mesh is 10 nm.

The gaseous fluid is assumed to be viscous because of a low Knudsen number for our geometry in atmospheric pressure. Module 3 does not include electron impact reactions but calculates only the reactions listed in Table II. The velocity of gaseous species in contact with the sliding substrate is assumed to be identical to the velocity of the substrate, which is called the *nonslip* condition in fluid dynamics.[49] The influx of each species fed from the DBD region is given by the product of its flow velocity of 10 m/s and its number density is taken from the steady-state results of module 2.

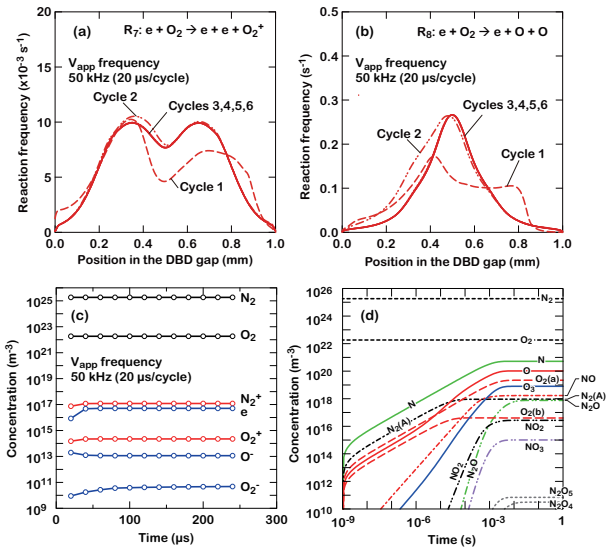

Fig. 2. (Color online) (a) Time-averaged spatial profiles of the reaction frequency of the electron impact ionization of O_2 (R7: $e + O_2 \rightarrow e + e + O_2^+$). (b) Time-averaged spatial profiles of the reaction frequency of the electron impact dissociation of O_2 (R8: $e + O_2 \rightarrow e + O + O$). (c) Spatially averaged densities of charged species obtained by discharge simulations performed for 12 cycles of the applied voltage. (d) Long-time-scale evolution of the concentrations of neutral species in the DBD region.

3. Results and discussion

3.1 Simulation in the DBD region

Figures 2(a) and 2(b) are examples of the results calculated using module 1, which show the spatial profiles of the frequencies of the electron-collision reactions E7 and E8 to ionize and dissociate O_2, respectively. Each profile is calculated by averaging the time evolution of the reaction frequencies over one cycle. The profiles for the first and second cycles are different from each other and show asymmetric spatial profiles even though these profiles are obtained by averaging over one cycle. This is due to the fact that the very initial condition is assumed to have no space charge or potential, while the later cycles are calculated from the data obtained at the end of the previous cycle. The profiles of the third cycle and later, on the other hand, are almost identical, which indicates that these reactions reach their periodic steady states after three cycles of DBD. Although the time evolution of all the reaction-frequency profiles is not shown, all the reactions in Table I reach their periodic steady states after three cycles. Such a tendency is reflected in the time evolution of the charged-species number densities shown in Fig. 2(c).

Figure 2(d) shows the results obtained using module 2, in which the number densities of all the species, except for the parent molecules N_2 and O_2, gradually increase and reach their

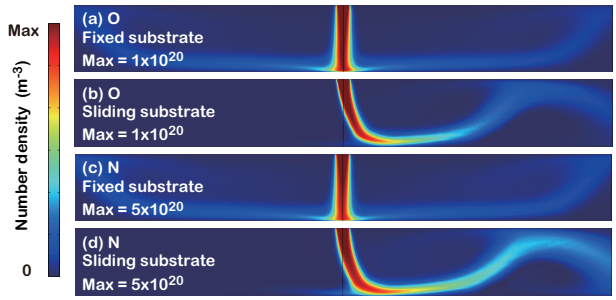

Fig. 3. (Color online) Spatial profiles of the number density of atomic oxygen in the flow channel (a) on the fixed substrate and (b) on the sliding substrate, and those of the number density of atomic nitrogen (c) on the fixed substrate and (d) on the sliding substrate. The ambient gas is air for all cases. The height and length of the flow channel are 5 and 40 mm, respectively.

steady states at approximately 5 ms. The number densities at 5 ms, which corresponds to the mean residence time in the DBD region, are used to calculate influxes into the flow channel from the DBD region in module 3. The number densities of the parent molecules do not show marked reduction under this condition, which allows us to assume a uniform number density of the parent molecules in the entire DBD region.

3.2 Reduction in the fluxes of atomic oxygen and nitrogen owing to the gas-drag effect

In this subsection, we discuss the results of 2D simulation in the flow channel irradiated with the DBD-APPJ in terms of the gas-drag effect caused by the sliding substrate. Figures 3(a) and 3(b) show spatial profiles of the number density of atomic oxygen on the fixed and sliding substrates, respectively. Figures 3(c) and 3(d) show those of atomic nitrogen.

On the fixed substrate, atomic oxygen and nitrogen perpendicularly impinge on the substrate surface and symmetrically spread to both the left- and right-hand sides. On the sliding substrate, on the other hand, the spatial profiles of the number density of atomic oxygen and nitrogen are asymmetric. This is due to the gas-drag effect, in which the sliding substrate drags gaseous species in contact with it and alters their flow trajectories.

Although the flow trajectory of atomic oxygen appears similar to that of atomic nitrogen, atomic oxygen is lost at a higher rate than atomic nitrogen in the vicinity of the sliding substrate. This tendency is clearly demonstrated by the characteristics of their fluxes on the substrate, as shown in Figs. 4(a) and 4(b), in which the data in N_2 ambient are for comparison and will be discussed later. The flux for each species was calculated as the sum of normal components of diffusive and convective fluxes on the surface. Since the diffusive flux is approximately 5 orders of magnitude greater than the convective flux, the flux is mostly

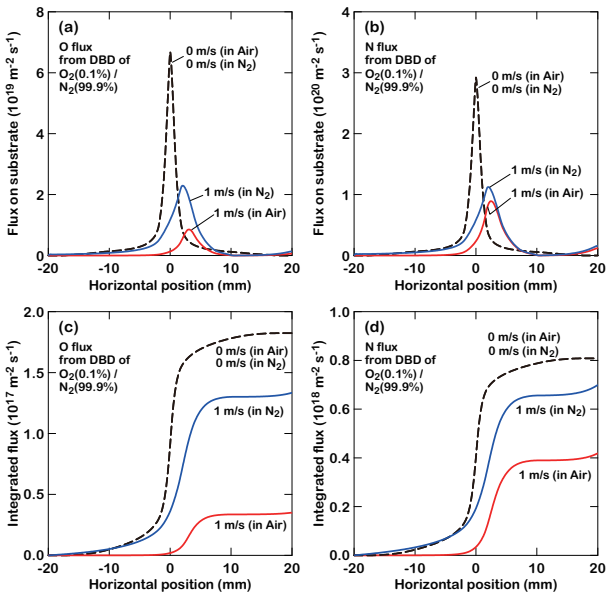

Fig. 4. (Color online) Flux of (a) atomic oxygen and (b) atomic nitrogen on the fixed and sliding substrates in ambient air and N_2. Integrated flux of (c) atomic oxygen and (d) atomic nitrogen on the fixed and sliding substrates in ambient air and N_2.

governed by the diffusive flux. The flux of atomic oxygen on the fixed substrate shows the highest value at the center where the APPJ is irradiated. On the sliding substrate, the peak position of the flux shifts to the right, and the absolute value of the peak flux is reduced to 13% of that on the fixed substrate. A similar tendency is also seen in the flux of atomic nitrogen. However, the peak flux of atomic nitrogen on the sliding substrate, which is approximately 31% of that on the fixed substrate, is larger than that of atomic oxygen. Since the fluxes integrated over all horizontal positions also show the same tendency, this difference is not explained by the difference in the broadening of the flux distribution but by the difference in the loss rates of atomic oxygen and nitrogen. To determine the reasons why atomic oxygen shows a higher loss rate than atomic nitrogen, we have analyzed the spatial distributions of reaction kinetics in the flow channel.

3.3 Mechanisms of reduction in the fluxes of atomic oxygen and nitrogen

Atomic oxygen is lost through reactions R3, R5, R7, R10, R11, R22, R23, R24, R37, and R44 (Table II). Figure 5(a) shows the rates of these reactions at the center of the flow channel on the fixed substrate. The major reactions that govern the total atomic oxygen loss rate are R3, R7, and R11, among which, R3 shows the highest loss rate. Figure 5(b) shows the atomic oxygen loss rates on the sliding substrate; the spatial profiles of the reaction rates significantly differ from those in Fig. 5(a) for the fixed substrate. In addition, the absolute R3 rate markedly

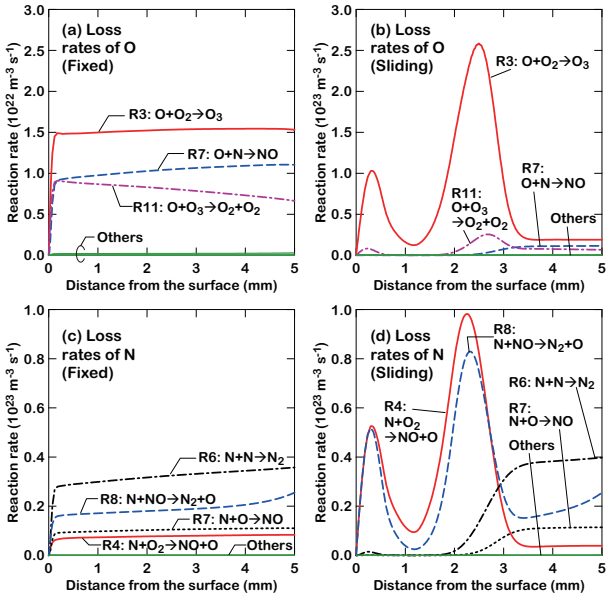

Fig. 5. (Color online) Spatial profiles of the atomic oxygen loss reaction rates on the vertical line at the horizontal center of the flow channel (a) on the fixed and (b) the sliding substrates. (c) and (d) are those of the atomic nitrogen loss reaction rates. The ambient gas is air for all cases.

increases from 1.5×10^{22} m^{-3} s^{-1} on the fixed substrate to 2.5×10^{23} m^{-3} s^{-1} on the sliding substrate. The marked difference in atomic oxygen loss rates is explained by the increase in the rate of R3 owing to the gas-drag effect upon externally supplying O_2.

In the case of the fixed substrate, the number density of O_2 is governed by the APPJ, in which the O_2 concentration is only 0.1%. Since atomic oxygen is lost through R3, which requires O_2, this situation resulted in the low atomic oxygen loss reaction rate. In the case of the sliding substrate, on the other hand, ambient air is fed from the left-hand side of the flow channel owing to the gas-drag effect. Figures 6(a)–6(d) show the spatial distributions of N_2 and O_2 mole fractions in the flow channel on the sliding substrate, in which 20% O_2 is dragged into the flow channel and distributed on the left-hand side of the APPJ. This additional O_2 contributes to R3 and increases the loss rate of atomic oxygen and causes the significant loss of atomic oxygen on the sliding substrate. On the other hand, the spatial distributions of N_2 and O_2 mole fractions are uniform on the fixed substrate, as shown in Figs. 6(e)–6(h), because the entire flow channel including both the left- and right-hand sides is filled with the gas mixture of 99% N_2 and 1% O_2 effused from the APPJ on the fixed substrate.

The loss reactions for atomic nitrogen are R4, R6, R7, R8, R9, R16, R17, R18, R19, and R36 in Table II. Figure 5(c) shows the rates of these reactions at the center of the flow channel on the fixed substrate. The major reactions that govern the total atomic nitrogen loss rate are

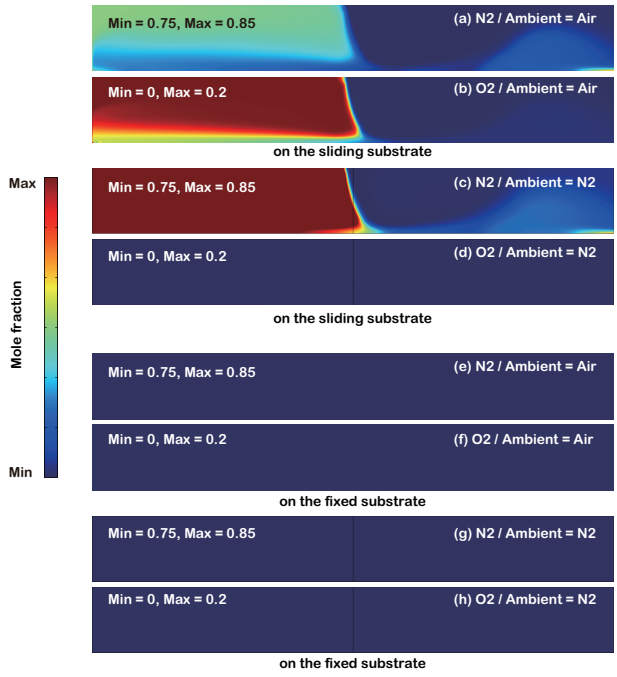

Fig. 6. (Color online) Spatial distributions of (a) N_2 and (b) O_2 in air ambient on the sliding substrate, and (c) N_2 and (d) O_2 in N_2 ambient on the sliding substrate. Spatial distributions of (e) N_2 and (f) O_2 in air ambient on the fixed substrate, and (g) N_2 and (h) O_2 in N_2 ambient on the fixed substrate.

R4, R6, R7, and R8. In the case of the fixed substrate, R6 indicates the highest loss rate, as shown in Fig. 5(c). In the case of the sliding substrate, as shown in Fig. 5(d), the dominant atomic nitrogen loss reactions rapidly turn into R4 and R8 near the surface. However, the absolute loss rates of atomic nitrogen on the sliding substrate remain on the same order of magnitude as those on the fixed substrate.

As discussed above, the sliding substrate has different effects on the loss mechanisms of atomic oxygen and nitrogen. This tendency is also observed in the 2D spatial distributions of R3, R4, and R6 shown in Fig. 7. In the case of the fixed substrate, the loss rates have laterally symmetric profiles for both atomic oxygen and nitrogen. In the case of the sliding substrate, the spatial profiles of the loss rates were markedly altered by the gas-drag effect. In addition, since the APPJ in the flow channel is exposed to the dragged O_2 coming from the left-hand side, the rates of R3 and R4 are increased in the left-hand side of the APPJ. As discussed previously, the absolute loss rate of atomic oxygen increases by one order of magnitude upon sliding the substrate, while that of atomic nitrogen remains on the same order of magnitude. It should also be noted that the double-peak profiles in the loss rates shown in Figs. 5(b) and 5(d) appear as a consequence of slicing the 2D loss rate profiles bent by the gas-drag effect.

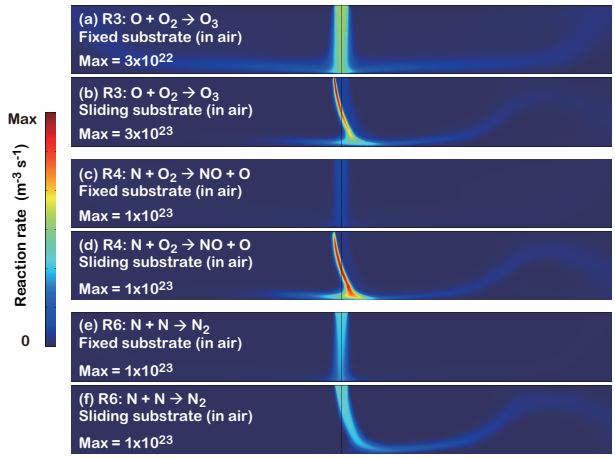

Fig. 7. (Color online) 2D spatial profiles of the reaction rates in the flow channel on the fixed and sliding substrates, where (a) and (b), (c) and (d), and (e) and (f) are those of R3, R4, and R6, respectively. The ambient gas is air for all cases. The height and length of the flow channel are 5 and 40 mm, respectively.

3.4 Effects of substituting ambient gas with N_2

According to the discussion in the previous subsection, reduction in the flux of atomic oxygen is caused by an excess supply of O_2, the source of which is the ambient air dragged by the sliding substrate. Thus, the loss of atomic oxygen is expected to be suppressed by removing O_2 in ambient air, that is, by changing the ambient gas from air to N_2. As a result, it is expected that the flux of atomic oxygen will increase, even on the sliding substrate.

As shown in Figs. 6(d) and 6(h), the mole fraction of O_2 is negligible in the cases of both a fixed and a sliding substrate if we change the ambient gas to N_2. Figures 8(a)–8(c) show 2D spatial profiles of R3, R4, and R6 respectively on the sliding substrate in N_2 ambient. Comparing Figs. 8(a) and 7(b), we can recognize that the atomic oxygen loss rates in N_2 ambient are reduced by one order of magnitude from those in air ambient. From Figs. 8(b) and 7(d), we can recognize also that the atomic nitrogen loss rates in N_2 ambient are reduced by one order of magnitude compared with those in air ambient.

The flux and the integrated flux of atomic oxygen on the sliding substrate in N_2 ambient are shown in Figs. 4(a) and 4(c), respectively. The peak flux was increased from 13 to 34% of that on the fixed substrate by changing the ambient gas from air to N_2. This increase appears to be small. However, it should be noted that the result of surface treatment for a sliding substrate is the sum of the effects at all positions in the horizontal channel. Thus, we have compared the integrated fluxes in Fig. 4(c), in which the integrated flux increases from 19 to 73% of that on the fixed substrate.

The increase of the peak flux of atomic nitrogen shown in Fig. 4(b) is only from 30 to

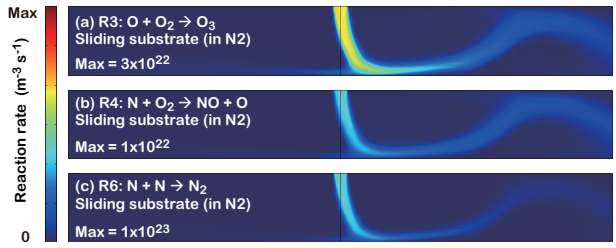

Fig. 8. (Color online) 2D spatial profiles of the rates of (a) R3, (b) R4, and (c) R6 on the sliding substrates in N_2 ambient. The height and length of the flow channel are 5 and 40 mm, respectively.

38%. The integrated flux shows a similar tendency in Fig. 4(d). Although it reaches 86% of the flux on the fixed substrate, the effects of changing the ambient gas from air to N_2 are not as marked on atomic nitrogen as of those on atomic oxygen. This is due to the fact that atomic nitrogen loss rates are not as affected by externally supplied O_2 as atomic oxygen loss rates, which has already been discussed above.

4. Conclusions

We performed numerical simulations of the reaction kinetics and flow dynamics of the APPJ of a N_2/O_2 gas mixture in a 2D flow channel with a height of 5 mm and investigated the effects of a sliding substrate and changing the ambient gas. The sliding substrate in the flow channel causes the gas-drag effect. The gas-drag effect not only alters the APPJ trajectory but also causes a significant loss of atomic oxygen in air ambient. The atomic oxygen flux integrated on the substrate is reduced to 19% of that on the fixed substrate owing to the increase in the atomic oxygen loss reaction rates, which is caused by the external supply of O_2 in air. In contrast, the reduction in the atomic nitrogen flux is not as severe as that of atomic oxygen because O_2 contributes less to the loss mechanism of atomic nitrogen. The unfavorable gas-drag effects can be suppressed by changing the ambient gas from air to N_2. The integrated flux of atomic oxygen on the sliding substrate was increased to 73% of that on the fixed substrate.

Acknowledgments

This work was partly supported by JSPS/MEXT KAKENHI Grant Numbers 15H03585 and 15K13391.

References

1) K. Gotoh, A. Yasukawa, and Y. Kobayashi, Polym. J. **43**, 545 (2011).
2) T. Shirafuji, M. Iwamura, R. Taga, Y. Kashiwagi, K. Nakajima, Y. Ogata, K. Tanaka, A. Tachibana, and T. Tanabe, Jpn. J. Appl. Phys. **55**, 07LG03 (2016).
3) M. C. Kim, S. H. Yang, J. H. Boo, and J. G. Han, Surf. Coatings Technol. **174-175**, 839 (2003).
4) C. H. Yi, T. W. Kim, K.-H. Kim, W. S. Kang, J. H. Kim, and S. K. Hong, Jpn. J. Appl. Phys. **47**, 6965 (2008).
5) A. West, M. van der Schans, C. Xu, M. Cooke, and E. Wagenaars, Plasma Sources Sci. Technol. **25**, 02LT01 (2016).
6) M. J. Kushner, J. Phys. D **38**, 1633 (2005).
7) G. V. Naidis, Appl. Phys. Lett. **98**, 141501 (2011).
8) T. Murakami, K. Niemi, T. Gans, D. O'Connell, and W. G. Graham, Plasma Sources Sci. Technol. **22**, 015003 (2013).
9) S. A. Norberg, E. Johnsen, and M. J. Kushner, J. Phys. D **49**, 185201 (2016).
10) S. Meiners, J. G. H. Salge, E. Prinz, and F. Förster, Surf. Coatings Technol. **98**, 1121 (1998).
11) P. J. Bruggeman, M. J. Kushner, B. R. Locke, J. G. E. Gardeniers, W. G. Graham, D. B. Graves, R. C. H. M. Hofman-Caris, D. Maric, J. P. Reid, E. Ceriani, D. F. Rivas, J. E. Foster, S. C. Garrick, Y. Gorbanev, S. Hamaguchi, F. Iza, H. Jablonowski, E. Klimova, J. Kolb, F. Krcma, P. Lukes, Z. Machala, I. Marinov, D. Mariotti, S. M. Thagard, D. Minakata, E. C. Neyts, J. Pawlat, Z. L. Petrovic, R. Pflieger, S. Reuter, D. C. Schram, S. Schröter, M. Shiraiwa, B. Tarabová, P. A. Tsai, J. R. R. Verlet, T. von Woedtke, K. R. Wilson, K. Yasui, and G. Zvereva, Plasma Sources Sci. Technol. **25**, 053002 (2016).
12) P. Bruggeman and C. Leys, J. Phys. D **42**, 053001 (2009).
13) A. V. Phelps and L. C. Pitchford, Phys. Rev. A **31**, 2932 (1985).
14) G. G. Raju, *Gaseous Electronics Tables, Atoms, and Molecules* (CRC Press, Boca Raton, FL, 2012) Chap. 25, p. 159.
15) P. C. Cosby, J. Chem. Phys. **98**, 9544 (1993).
16) S. A. Lawton and A. V. Phelps, J. Chem. Phys. **69**, 1055 (1978).
17) G. G. Raju, *Gaseous Electronics Tables, Atoms, and Molecules* (CRC Press, Boca Raton, FL, 2012) Chap. 26, p. 169.
18) G. J. M. Hagelaar and L. C. Pitchford, Plasma Sources Sci. Technol. **14**, 722 (2005).

19) F. J. Gordillo-Vázquez, J. Phys. D **41**, 234016 (2008).
20) H. Akashi, Y. Sakai, N. Takahashi, and T. Sasaki, J. Phys. D **32**, 2861 (1999).
21) F. Tochikubo, S. Uchida, H. Yasui, and K. Sato, Jpn. J. Appl. Phys. **48**, 076507 (2009).
22) F. Tochikubo, Thin Solid Films **518**, 957 (2009).
23) A. Mizuno, K. Shimizu, A. Chakrabarti, L. Dascalescu, and S. Furuta, IEEE Trans. Ind. Appl. **31**, 957 (1995).
24) I. Stefanović, N. K. Bibinov, A. A. Deryugin, I. P. Vinogradov, A. P. Napartovich, and K. Wisemann, Plasma Sources Sci. Technol. **10**, 406 (2001).
25) G.-B. Zhao, X. Hu, M. D. Argyle, and M. Radosz, Ind. Eng. Chem. Res. **43**, 5077 (2004).
26) D. P. Bakker, A. van der Plaats, G. J. Verkerke, H. J. Busscher, and H. C. van der Mei, Appl. Environ. Microbiol. **69**, 6280 (2003).
27) W. A. Cole and W. A. Wakeham, J. Phys. Chem. Ref. Data **14**, 209 (1985).
28) L. A. Rosocha, in *Plasma Science and the Environment*, ed. W. Manheimer, L. E. Sugiyama, and T. H. Stix (AIP Press, Woodbury, NY, 1997) Chap. 11, p. 261.
29) D. L. Baulch, R. A. Cox, P. J. Crutzen, R. F. Hampson Jr., J. A. Kerr, J. Troe, and R. T. Watson, J. Phys. Chem. Ref. Data **11**, 327 (1982).
30) J. C. Person and D. O. Ham, Radiat. Phys. Chem. **31**, 1 (1988).
31) R. Atkinson, D. L. Baulch, R. A. Cox, R. F. Hampson, Jr., J. A. Kerr, M. J. Rossi, and J. Troe, J. Phys. Chem. Ref. Data **26**, 1329 (1997).
32) M. Capitelli, C. M. Ferreira, B. F. Gordiets, and A. I. Osipov, *Plasma Kinetics in Atmospheric Gases* (Springer, Berlin, 2000) Chap. 10.
33) W. Tsang and R. F. Hampson, J. Phys. Chem. Ref. Data **15**, 1087 (1986).
34) M. A. A. Clyne and D. H. Stedman, J. Phys. Chem. **71**, 3071 (1967).
35) I. M. Campbell and C. N. Gray, Chem. Phys. Lett. **18**, 607 (1973).
36) W. B. DeMore, S. P. Sander, D. M. Golden, R. F. Hampson, M. J. Kurylo, C. J. Howard, A. R. Ravishankara, C. E. Kolb, and M. J. Molina, JPL Publication 97-4 (Jet Propulsion Laboratory, Pasadena, CA, 1997) p. 18.
37) R. Atkinson, D. L. Baulch, R. A. Cox, R. F. Hampson, J. A. Kerr, and J. Troe, J. Phys. Chem. Ref. Data **18**, 881 (1989).
38) R. Atkinson, D. L. Baulch, R. A. Cox, J. N. Crowley, R. F. Hampson, R. G. Hynes, M. E. Jenkin, M. R. Rossi, and J. Troe, Atmos. Chem. Phys. **4**, 1461 (2004).
39) J. Hjorth, J. Notholt, and G. Restelli, Int. J. Chem. Kinet. **24**, 51 (1992).
40) V. Y. Bazhenov, A. V. Ryabtsev, I. A. Soloshenko, V. A. Khomich, V. V. Tsiolko, A. I.

Shchedrin, A. I. Kuzmichev, V. I. Kryzhanovsky, and I. L. Mikhno, Ukr. J. Phys. **48**, 27 (2003).

41) L. F. Phillips and H. I. Schiff, J. Chem. Phys. **42**, 3171 (1965).
42) T. J. Wallington and S. M. Japar, J. Atmos. Chem. **9**, 399 (1989).
43) I. A. Kossyi, A. Y. Kostinsky, A. A. Matveyev, and V. P. Silakov, Plasma Sources Sci. Technol. **1**, 207 (1992).
44) D. X. Liu, P. Bruggeman, F. Iza, M. Z. Rong, and M. G. Kong, Plasma Sources Sci. Technol. **19**, 025018 (2010).
45) D. S. Stafford and M. J. Kushner, J. Appl. Phys. **96**, 2451 (2004).
46) L. Deng, W. Shi, H. Yang, G. Sha, and C. Zhang, Rev. Sci. Instrum. **75**, 4455 (2004).
47) E. C. Zipf, Can. J. Chem. **47**, 1863 (1969).
48) K. Becker, M. Schmidt, A. A. Viggiano, R. Dressler, and S. Williams, in *Non-equilibrium Air Plasmas at Atmospheric Pressure*, ed. K. H. Becker, U. Kogelschatz, K. H. Schoenbach, and R. J. Barker (IOP Publishing, Bristol, U.K., 2005) Chap. 4, p. 124.
49) G. K. Batchelor, *An Introduction to Fluid Dynamics* (Cambridge University Press, Cambridge, U.K., 1967) Chap. 3, p. 131.